Reversible inhibition of the ClpP protease via an N-terminal conformational switch

Siavash Vahidi[a,b,c,d,1], Zev A. Ripstein[b,d,1], Massimiliano Bonomi[e], Tairan Yuwen[a,b,c,d], Mark F. Mabanglo[b], Jordan B. Juravsky[d], Kamran Rizzolo[b], Algirdas Velyvis[a,b,c,d], Walid A. Houry[b,c], Michele Vendruscolo[e], John L. Rubinstein[b,d,f,2], and Lewis E. Kay[a,b,c,d,2]

[a]Department of Molecular Genetics, University of Toronto, Toronto, ON M5S 1A8, Canada; [b]Department of Biochemistry, University of Toronto, Toronto, ON M5S 1A8, Canada; [c]Department of Chemistry, University of Toronto, Toronto, ON M5S 1A8, Canada; [d]Program in Molecular Medicine, The Hospital for Sick Children, Toronto, ON M5G 1X8, Canada; [e]Centre for Misfolding Diseases, Department of Chemistry, University of Cambridge, CB2 1EW Cambridge, United Kingdom; and [f]Department of Medical Biophysics, University of Toronto, Toronto, ON M5G 1L7, Canada

Edited by Gerhard Wagner, Harvard Medical School, Boston, MA, and approved May 25, 2018 (received for review March 23, 2018)

Protein homeostasis is critically important for cell viability. Key to this process is the refolding of misfolded or aggregated proteins by molecular chaperones or, alternatively, their degradation by proteases. In most prokaryotes and in chloroplasts and mitochondria, protein degradation is performed by the caseinolytic protease ClpP, a tetradecamer barrel-like proteolytic complex. Dysregulating ClpP function has shown promise in fighting antibiotic resistance and as a potential therapy for acute myeloid leukemia. Here we use methyl–transverse relaxation-optimized spectroscopy (TROSY)–based NMR, cryo-EM, biochemical assays, and molecular dynamics simulations to characterize the structural dynamics of ClpP from *Staphylococcus aureus* (SaClpP) in wild-type and mutant forms in an effort to discover conformational hotspots that regulate its function. Wild-type SaClpP was found exclusively in the active extended form, with the N-terminal domains of its component protomers in predominantly β-hairpin conformations that are less well-defined than other regions of the protein. A hydrophobic site was identified that, upon mutation, leads to unfolding of the N-terminal domains, loss of SaClpP activity, and formation of a previously unobserved split-ring conformation with a pair of 20-Å-wide pores in the side of the complex. The extended form of the structure and partial activity can be restored via binding of ADEP small-molecule activators. The observed structural plasticity of the N-terminal gates is shown to be a conserved feature through studies of *Escherichia coli* and *Neisseria meningitidis* ClpP, suggesting a potential avenue for the development of molecules to allosterically modulate the function of ClpP.

ClpP | conformational dynamics | allostery | methyl-TROSY NMR | cryo-EM

Timely and targeted removal of damaged and misfolded proteins as well as proteins that must be cleared upon completion of a prescribed function is essential for cellular viability (1). In many prokaryotes and in mitochondria, protein degradation is performed by caseinolytic protease (ClpP) (2–6). In bacteria, ClpP is associated with the regulation of the cellular stress response, homeostasis, pathogenesis, intracellular parasitism, and virulence (7–9). Given its extensive role in bacterial cells, ClpP represents an important but mostly untapped drug target (10, 11). Therefore, there is significant interest in the development of methods for modulating its activity via either inhibition or activation (12, 13). An emerging class of antibiotics, cyclic acyldepsipeptides (ADEPs) (14) and activators of cylindrical proteases (ACPs) (15), bind to and induce unregulated proteolytic activity in bacterial ClpPs, thereby resulting in the degradation of proteins critical for bacterial survival (16). This novel mode of action was shown to kill *Mycobacterium tuberculosis* (17) and antibiotic-resistant subpopulations of *Staphylococcus aureus* that are implicated in chronic and relapsing infections (18). Similarly, an increasing number of compounds including β-lactones and phenyl esters have been shown to inhibit ClpP function in bacteria (19), and some of these have been proposed for the treatment of malaria by targeting ClpP from the malaria parasite (20). Much less is known about the function of ClpP in mitochondria. Mitochondrial ClpP is overexpressed in human cancer cells, enabling metastasis (21), and its inhibition has shown promise in treating acute myeloid leukemia (22). Further, mutations in mitochondrial ClpP are found in patients with Perrault syndrome (23), an autosomal recessive condition associated with hearing loss and ovarian dysgenesis (24). Understanding the structure, function, and regulation of this protease will facilitate further development of effective therapeutics to combat a wide range of disorders affecting human health (17).

Detailed X-ray crystallographic studies of most bacterial ClpPs show they consist of a pair of stacked homoheptameric rings in a barrel-like structure, sequestering 14 Ser-His-Asp catalytic sites (Fig. 1*A*) (25–27). Each ClpP subunit is comprised of three domains: (*i*) an N-terminal region surrounding gated narrow axial pores (Fig. 1 *B* and *C*) that regulate access to the degradation

Significance

ClpP is a protease that degrades damaged or misfolded proteins. Consistent with its critical role in maintaining cellular homeostasis, inhibiting and dysregulating ClpP function has shown promise in fighting antibiotic resistance and in targeting cancer cells in acute myeloid leukemia. Here we identify a conformational switch in ClpP that, upon mutagenesis, leads to a catalytically inactive structure that can be reactivated through the binding of small-molecule activators. This functional hotspot therefore represents a drug target for allosteric inhibition of ClpP. The combination of methyl–transverse relaxation-optimized spectroscopy (TROSY) NMR, cryo-EM, and molecular simulation methods employed here provides a detailed characterization of ClpP along with the promise of crucial insights into the structure–function relationship of molecular machines in general.

Author contributions: S.V. and L.E.K. initiated the project; S.V., Z.A.R., M.B., W.A.H., M.V., J.L.R., and L.E.K. designed research; S.V., Z.A.R., M.B., J.B.J., A.V., and L.E.K. performed research; T.Y., M.F.M., K.R., and A.V. contributed new reagents/analytic tools; S.V., Z.A.R., M.B., T.Y., and L.E.K. analyzed data; S.V., Z.A.R., J.L.R., and L.E.K. wrote the paper; M.V. supervised molecular dynamics studies; J.L.R. supervised the electron cryomicroscopy studies; and L.E.K. supervised NMR studies.

The authors declare no conflict of interest.

This article is a PNAS Direct Submission.

Data deposition: Electron microscopy density maps have been deposited in the Electron Microscopy Databank (accession nos. EMD-7950–EMD-7952). Atomic models have been deposited in the Protein Databank (PDB ID code 6DKF).

[1]S.V. and Z.A.R. contributed equally to this work.

[2]To whom correspondence may be addressed. Email: john.rubinstein@utoronto.ca or kay@pound.med.utoronto.ca.

This article contains supporting information online at www.pnas.org/lookup/suppl/doi:10.1073/pnas.1805125115/-/DCSupplemental.

Published online June 25, 2018.

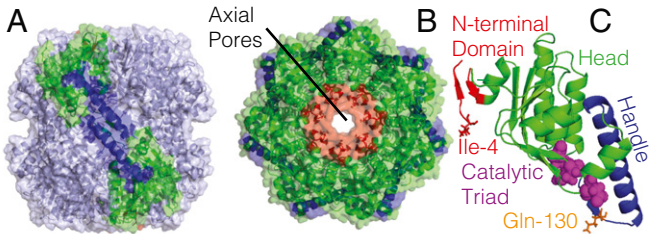

Fig. 1. Architecture of the tetradecameric ClpP structure [Protein Data Bank (PDB) ID code 3V5E (54)]. (*A* and *B*) Surface representation of the extended form of SaClpP as seen from side (*A*) and top (*B*). The N-terminal domains are shown in red, and the head and handle domains appear in green and blue, respectively. (*C*) Cartoon representation of the structure of an individual SaClpP protomer highlighting the N-terminal, head, and handle regions. The positions of Ile-4, the catalytic triad, and the site chosen for attachment of the spin label (Gln-130) within each protomer are indicated.

chamber (28); (*ii*) a globular head domain that forms the main body of the barrel; and (*iii*) a handle domain that forms the ring–ring interface of the ClpP tetradecamer. Analogous to the proteasome, ClpP collaborates with AAA+ (ATPases associated with a variety of cellular activities) unfoldases, including ClpA, ClpC, and ClpX, to unfold substrates and translocate them into the catalytic chamber of ClpP in an ATP-dependent manner (29, 30).

There is significant evidence from a variety of different biophysical techniques that ClpP is a highly dynamic molecular complex. For example, ClpP can be crystallized in three distinct conformations (4), including extended (25, 26, 31), compact (32, 33), and compressed (31, 34, 35) forms that differ in the height of the barrel and in the conformation of the handle region. Further insight comes from NMR studies focusing on a pair of Ile residue probes showing the presence of at least two handle-region conformations in solution (36). Molecular dynamics (MD) simulations (37) and normal-mode analysis (32) also suggest a dynamic system, with interconversion between extended and compact forms of the enzyme. A comparison of available crystal structures further reveals a high degree of heterogeneity in the N-terminal region (5) and disorder in many cases (25, 26, 38). When the N-terminal residues are observed crystallographically, they assume an antiparallel β-hairpin conformation that protrudes from the apical surface of the barrel, although there is some question as to whether this structure is an artifact arising from crystal contacts (4, 5).

Despite the wealth of available structural information, a rigorous understanding of the connection between the inherent plasticity of ClpP and its function is lacking. The processive nature of proteolysis by ClpP (39) and the coordinated mode of action between protease and unfoldase (40) suggest a role for allostery. For example, the N-terminal region of ClpP interacts with the pore-2 loops of the unfoldase (41, 42), while binding of AAA+ unfoldases or activators and the introduction of gain-of-function mutations have been shown to enhance substrate hydrolysis rates of ClpP (43–45). The interaction between ClpP and unfoldase thus leads to changes in catalytic rates at distal sites in both molecules. While the N-terminal gating regions of ClpP must play a central role in this allosteric process, their structural dynamics remain to be characterized in detail, and the mechanism of communication between the N terminus and the rest of the protein, including potential hotspots of interaction, have yet to be established.

Here we build on our original NMR study, which focused on a pair of Ile probes in the handle region of ClpP (36), to study the structural dynamics of the N-terminal residues and the communication between them and other regions of the molecule. For this work we use ClpP from *Staphylococcus aureus* (SaClpP). The development of robust methyl labeling protocols (46, 47) in concert with NMR methods that exploit a methyl-transverse relaxation optimized spectroscopy (TROSY) effect (48) provide an avenue for studies of large molecular machines (49, 50), including the 300-kDa ClpP protease. We present nearly complete NMR assignments for Ile, Leu, Val, and Met methyl groups in SaClpP to generate probes of structure and dynamics throughout the enzyme. Extensive conformational heterogeneity is observed for the N-terminal gates, extending to the active-site and handle regions, with approximately 10 distinct cross-peaks assigned for Ile-4 and for Ile-8 in ^{1}H-^{13}C heteronuclear multiple-quantum coherence (HMQC) spectra. Conformational heterogeneity was further characterized via paramagnetic relaxation enhancement (PRE) experiments and through the determination of a 3.6-Å resolution cryo-EM structure of the WT protein that showed an extended conformation with gates in the predominantly β-hairpin form, long thought to be a crystal contact artifact. Modeling based on MD simulations using restraints from the cryo-EM density (51, 52) generated an ensemble of structures showing increased dynamics in the N-terminal domain. Truncation of as few as three N-terminal residues or a V7A substitution led to the complete unfolding of the gating residues and the identification of an important structural hotspot that involves a well-conserved hydrophobic cluster comprising residues near the N-terminal domain. The cryo-EM structure of the V7A mutant reveals the formation of a heretofore unobserved split-ring conformation that is catalytically inactive, although activity could be restored through binding of activators. Remarkably, a single V7A mutation in one of the 14 protomers is sufficient to unfold all N-domains in the tetradecamer and eliminate catalytic activity, emphasizing both the importance of the integrity of this region for proper function and the strong communication between protomers. Finally, the observed structural plasticity at the level of the N-terminal gates observed for SaClpP is shown to be a conserved feature through studies of *Escherichia coli* and *Neisseria meningitidis* ClpP, suggesting a potential avenue for further rational development of molecules to modulate the function of this important enzyme.

Results

Conformational Heterogeneity Is Predominant in the N-Terminal Region of WT SaClpP. To study the structural plasticity of the 300-kDa SaClpP tetradecamer, we used a well-described strategy that focuses on methyl probes in which highly deuterated protein is prepared and labeled as [U-^{2}H; Ileδ1-$^{13}CH_3$; Leu/Val-$^{13}CH_3$/$^{12}CD_3$; Met-$^{13}CH_3$], hereafter referred to as "ILVM labeling" (46). The labeling approach was exploited by recording ^{1}H-^{13}C HMQC spectra that take advantage of a methyl-TROSY effect (48) and allow studies of high molecular weight complexes. Nearly complete resonance assignments of Ile, Leu, Val, and Met methyl probes (51 of 53) in a spectrum of ILVM-SaClpP were obtained through a combined approach involving single-point mutagenesis and analysis of NOE datasets (53), aided by the availability of high-resolution X-ray structures of SaClpP (31, 54). Fig. 2*A* shows the Ile region of a 2D ^{1}H-^{13}C HMQC spectrum of SaClpP recorded at 40 °C and 18.8 T. Corresponding regions and assignments for Leu, Val, and Met methyl groups are shown in *SI Appendix*, Fig. S1 *A* and *B* along with stereospecific assignments for the isopropyl methyl groups of Leu and Val obtained using the labeling approach of Gans et al. (55).

Notably, more peaks were observed in the HMQC spectrum than would be expected on the basis of the number of ILVM-methyl groups in the protein (Fig. 2*A* and *SI Appendix*, Fig. S1 *A* and *B*). This discrepancy is particularly pronounced for methyl-containing residues localized to the N-terminal domain where, for example, approximately 10 correlations each were assigned to Ile-4 (Fig. 2*A*, pink) and to Ile-8 (Fig. 2*A*, green), spanning *ca.* 0.7 ppm and 2.5 ppm in the ^{1}H and ^{13}C dimensions, respectively. Because of the surprisingly large number of cross-peaks in these cases, the assignments were verified by recording spectra of samples in which each of the 22 Ile residues was individually mutated to Val. All the peaks assigned to Ile-4 remained in each

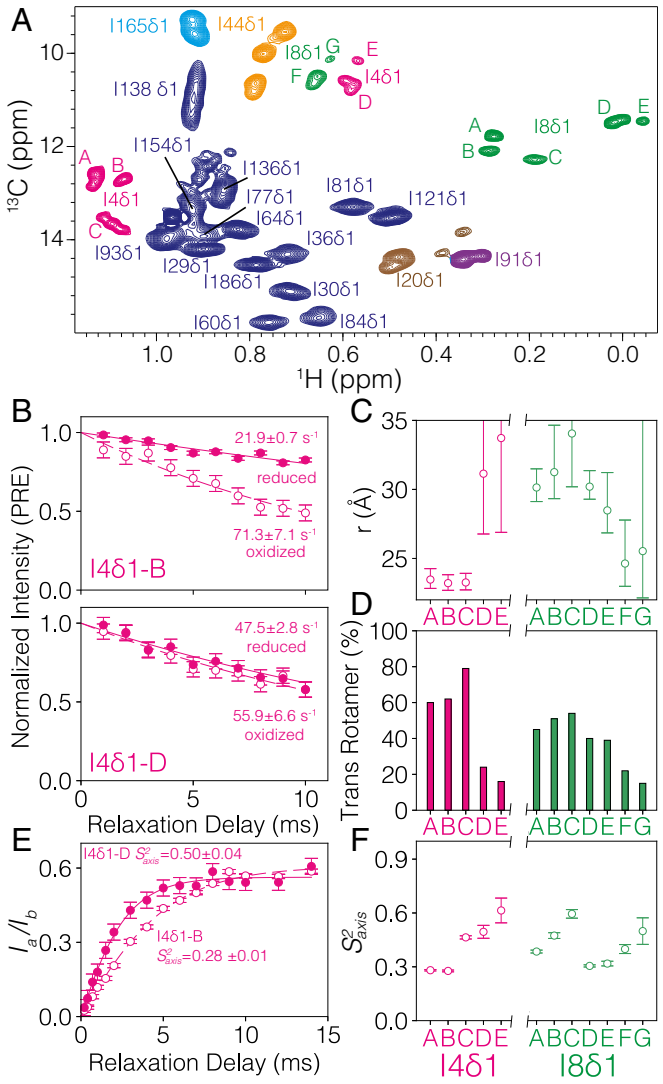

Fig. 2. NMR studies reveal multiple conformers, especially for the N-domain. (*A*) The Ile region of a ^{1}H-^{13}C HMQC correlation map of WT SaClpP, 40 °C, 18.8 T, with assignments. Peaks derived from the same residue are colored identically. (*B*) Representative decay curves for the slowly relaxing component of methyl ^{1}H transverse magnetization (circles) along with fits (solid and dashed curves) for a pair of Ile-4 peaks for spin-label oxidized (empty circles) and reduced states (filled circles). Relaxation rates and their uncertainties are displayed for each measurement. (*C*) Effective distances, *r*, between the C$^{\beta}$ carbon of position 130 (the site of attachment of a TEMPO maleimide spin label) and Ile-4/Ile-8 δ1 methyl groups from different conformers, as indicated. (*D*) Populations of Ile χ_2 *trans* rotameric states based on Ile ^{13}C$^{\delta1}$ chemical shifts of each of the conformers (56). (*E* and *F*) Representative profiles of ratios of peak intensities in triple-quantum–filtered (I_a) and single-quantum–based (I_b) ^{1}H relaxation experiments, I_a/I_b, as a function of relaxation delay (*E*) along with fits of data to extract the methyl axis order parameter S^2_{axis} plotted for the Ile-4 and Ile-8 δ1 methyl groups as a function of conformer (*F*).

spectrum except when Ile-4 was substituted (I4V), as did the peaks assigned to Ile-8. However, peak multiplicity is not limited to residues from the N-terminal region and includes probes distributed throughout the entire structure, such as Ile-44 from the head domain (Fig. 2*A*, orange), Met-99 proximal to the active-site Ser (*SI Appendix*, Fig. S1*B*, blue), and Ile-138 from the handle domain (Fig. 2*A*, blue) that are ∼8, 20, and 36 Å from the closest Ile-4 C$^{\delta1}$, respectively.

In an effort to discover the structural basis for the multiplicity of the observed correlations, in particular those from Ile-4 and Ile-8, we first carried out PRE experiments in which a nitroxide spin label was covalently attached to a Cys residue of the protein. Fig. 2*B* shows transverse relaxation decay profiles for selected peaks from Ile-4, focusing on the slowly relaxing component of methyl ^{1}H magnetization obtained with either an oxidized or reduced spin label placed at position 130 by mutating Gln-130 to Cys (Fig. 1*C*). The PRE, defined as the difference in relaxation rates measured in oxidized and reduced samples, can be used to calculate effective distances between the spin label and the methyl probe in question (*SI Appendix*), as tabulated for the various Ile-4 and Ile-8 peaks in Fig. 2*C*. Notably, distances vary by as much as 10 Å between the different conformers. It is worth noting that for methyl groups in well-ordered regions of ClpP good agreement between PRE-based distances and those calculated from the X-ray structure was obtained (*SI Appendix*, Fig. S1*C*), providing confidence in the measurements for Ile-4 and Ile-8. As a second probe of conformational heterogeneity, we exploited the sensitivity of the Ile ^{13}C$^{\delta1}$ chemical shift to the sidechain χ_2 dihedral angle to quantify *trans* χ_2 rotamer populations (56) for each of the Ile conformers and obtained a wide distribution of populations. Taken together, chemical shift and PRE data establish that both Ile-4 and Ile-8 exist in multiple conformations that are associated with significant differences in sidechain conformations and in the positions of Ile δ1 methyl groups relative to the core of the enzyme.

In an attempt to quantify the interconversion between conformers, we recorded magnetization exchange experiments that we have used successfully in the past for studies of the interconversion of N-terminal gates in the 20S proteasome (57). Notably, we were unable to detect exchange cross-peaks, even at temperatures as high as 50 °C. Calculations based on a simplified two-state exchange model establish an upper bound for the exchange rate of $\sim 0.1 \cdot s^{-1}$. Similarly, exchange dynamics were not detected via chemical exchange saturation transfer-based experiments (58). NMR spin relaxation measurements that are sensitive to picosecond-to-nanosecond timescale dynamics were also performed to probe amplitudes of motion of methyl-containing sidechains. In a previous study we showed that the proteasome gating termini were highly dynamic on a fast timescale (57), and we were interested in establishing whether the N termini of ClpP behave in a similar manner. ^{1}H triple-quantum–based experiments (59) were recorded from which an order parameter squared (S^2_{axis}) is obtained for each methyl group that reports on the amplitude of motion of the methyl symmetry axis. Values of the S^2_{axis} range, in the general case, from 1 (rigid) to 0 (isotropic motion); these values can be obtained from fits of ratios of signal intensities obtained in triple-quantum–selected (I_a) and single-quantum–based (I_b) experiments (Fig. 2*E*) (59) and are shown for Ile-4 and Ile-8 correlations in Fig. 2*F*. Notably, values range from 0.3 to 0.6, in the middle of the S^2_{axis} distribution observed for Ile in a series of folded proteins (from 0.1 to 0.8) (60) and are not significantly different from the S^2_{axis} value calculated by averaging across all probes in ClpP (∼0.45). This observation suggests that the Ile-4/Ile-8 methyl groups are, on average, as ordered as those in the rest of the structure and that the N-terminal region is not as mobile on the picosecond–nanosecond timescale as the gating residues of the proteasome.

Cryo EM of WT ClpP. The NMR results establish that the N-terminal domain of ClpP is structurally heterogeneous. In an effort to characterize the ClpP structure further, we used single-particle cryo-EM to obtain structural models of WT SaClpP. Ab initio structure determination and 3D classification with four classes was performed without imposing symmetry, resulting in a single class with the familiar ClpP barrel shape. Refinement of this 3D map while enforcing D7 symmetry resulted in a map at 3.6-Å resolution (Fig. 3*A* and *SI Appendix*, Fig. S2; see *SI Appendix* for details). Notably, the N-terminal region has a β-hairpin conformation with residues in the two-stranded β-sheet being well-ordered,

while those of the apical loop (Glu-9 – Arg-16) connecting the two β-strands are blurred in the density map. Further attempts to determine the distribution of conformations for the Glu9–Arg16 loop, including focused 3D classification by masking the N-terminal loop of a single protomer, did not result in interpretable classes. The failure of this attempt was likely due to the small amount of signal available from a seven-residue sequence of protein. When assessed for local resolution (61, 62), the N-terminal apical loop residues are estimated to have a resolution that is ∼2 Å worse than the global resolution of the structure, reflecting the dynamic nature of this region of ClpP.

Because the single unsymmetrized map derived from the cryo-EM data represents an ensemble average over conformations that reflect the N-terminal loop dynamics, we further analyzed the data with a metainference-based MD method (63) in which 24 replicas of ClpP were simulated in parallel, guided by the MD physiochemical force field used in standard MD simulations along with a second, much weaker force field that acts on each replica to correct the small differences between the predicted map, averaged over all replicas, and the experimental EM dataset (*SI Appendix*, Fig. S3) (52). This approach is fundamentally different from the popular MD flexible fitting (64) algorithm, which attempts to find the single atomic model that best fits the density map. In contrast, the approach we used attempts to find an ensemble of atomic models that best explain the variable resolution of the experimental map. Fig. 3*B* highlights a superposition of 100 structures from the ensemble of models that is consistent with the cryo-EM map of WT SaClpP, focusing on the N-terminal domain. Root mean squared fluctuations (RMSFs) of each residue, averaged over all backbone and sidechain atoms (excluding hydrogens) and over all members of the ensemble (circles), are shown in Fig. 3*C*. With the exception of the N-terminal domain (the first 20 residues) (Fig. 3*D*) and a few residues at the C terminus, WT SaClpP is relatively rigid with an average RMSF value of 0.66 Å, consistent with the input EM map. Notably, the ensemble is able to reproduce a number of important experimental observations. For example, as discussed above, distance fluctuations up to ∼10 Å are calculated between the Ile-4 and Ile-8 methyl groups and a spin-label attached at position 130 of the structure that is localized to the handle region of the ClpP barrel. A similar distance distribution is observed between Ile-4 and the center of mass of the enzyme in the ensemble (Fig. 3*E*), but for Ile-30 δ1 (head domain, Fig. 1*C*) a much more compact distribution is noted, consistent with the observation of only a single cross-peak in HMQC spectra for this methyl group. We have also used the program SHIFTX2 (65) to predict methyl ^{1}H-^{13}C spectra for a number of methyl groups on the basis of the ensemble of structures that were generated. The predicted chemical shifts for Ile-4, as well as for Ile-8, show at least three distinct clusters that differ in ^{1}H and ^{13}C chemical shifts (*SI Appendix*, Fig. S3*B*), analogous to the observations in experimental spectra, while only a single peak is predicted for Ile-30 δ1 (Fig. 3*C*), consistent with the experiment.

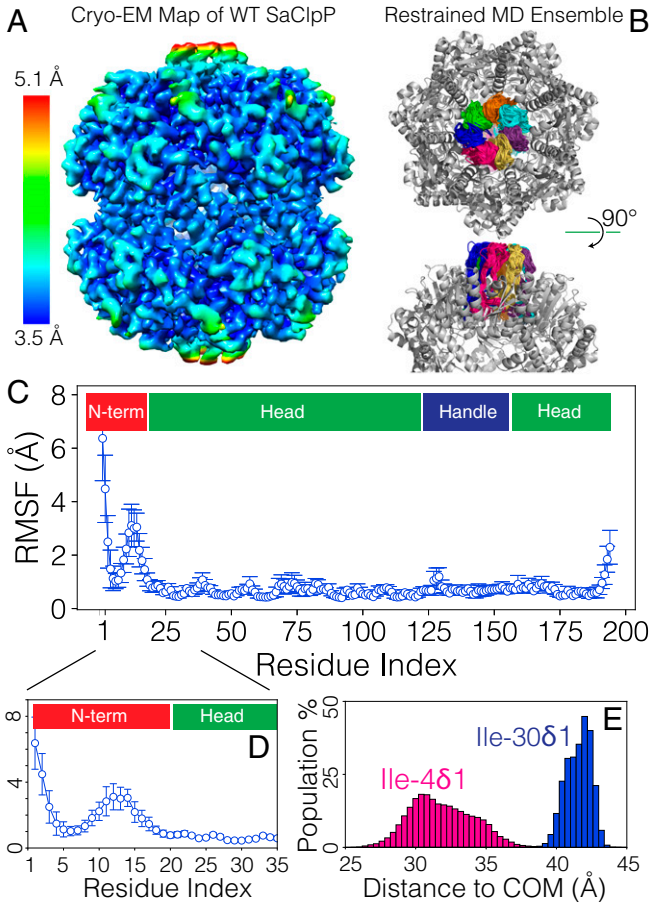

Fig. 3. The N-terminal domain is flexible. (*A*) Cryo-EM map of WT SaClpP at 3.6-Å resolution refined using D7 symmetry, with the distribution of local resolution color-coded as indicated. (*B*) The cryo-EM density was used to restrain metainference MD simulations of 24 replicas (52) and to generate a metainference ensemble consistent with the data; 100 structures for the N-domain, chosen randomly from the ensemble, are highlighted in separate colors for each protomer. Only a single ring is shown for simplicity. (*C* and *D*) RMSFs calculated for all heavy atoms of each residue from the ensemble of structures generated from restrained MD simulations. Mean values displayed (open circles) are averages over all 14 protomers; error bars represent one SD across the protomers. (*E*) Distribution of calculated distances from Ile-4 and Ile-30 to the center of mass (COM) of ClpP from the metainference ensemble.

Discovery of a Conformational Switch. During resonance assignment we identified a hydrophobic cluster at the interface of adjacent protomers near the apical surface of WT SaClpP whose perturbation due to mutation led to dramatic changes in NMR spectra. This cluster comprises Pro-5, Val-7, and Ile-20 from one protomer and Leu-25 and Phe-50 from an adjacent protomer (Fig. 4*A*), residues that are conserved across a large number of ClpPs (4). We used methyl-TROSY–based NMR to study structural perturbations caused by mutations within this cluster as illustrated in Fig. 4*B*, where an overlay of the Ile region of ^{1}H-^{13}C HMQC spectra recorded on samples of WT SaClpP (blue, single contour) and V7A SaClpP (pink, multicontour) is shown. All peaks belonging to N-terminal residues disappear for the V7A variant (Fig. 4*B*, *Inset 1*), with a dramatic increase in the intensity of peaks in the random coil region of the spectrum (Fig. 4*B*, *Inset 2*) suggestive of unfolding. Chemical shift perturbations extend throughout the entire ClpP tetradecameric structure; for example, Ile-44 (head domain), Ile-121 (proximal to the active site), and Ile-138 (handle domain) all show significant changes, and most residues in the V7A mutant appear as single peaks. We examined the spectra of other mutants within this cluster, including P5G, I20V, and constructs with three (Δ3; Asn-2–Ile-4) and 18 (Δ18; Asn-2–Asp-19) residues truncated from the N terminus. These spectra are similar to the spectrum of V7A SaClpP (*SI Appendix*, Fig. S4).

To assess the consequences of perturbing the N-terminal cluster, degradation assays were performed for different mutants by monitoring changes in fluorescence resulting from hydrolysis of a large excess of the fluorogenic substrate peptide *N*-Succinyl-Leu-Tyr-7-amino-4-methylcoumarin (LY-AMC) (Fig. 4*C*). The inactive S98A mutant, in which the catalytic Ser is replaced by Ala, was included as a control. Given the small size of the substrate, these assays report on the catalytic step and are not limited by substrate diffusion. We also carried out further functional assays using the 23-kDa disordered α-casein as substrate, which report on both the degree to which the substrate can access the

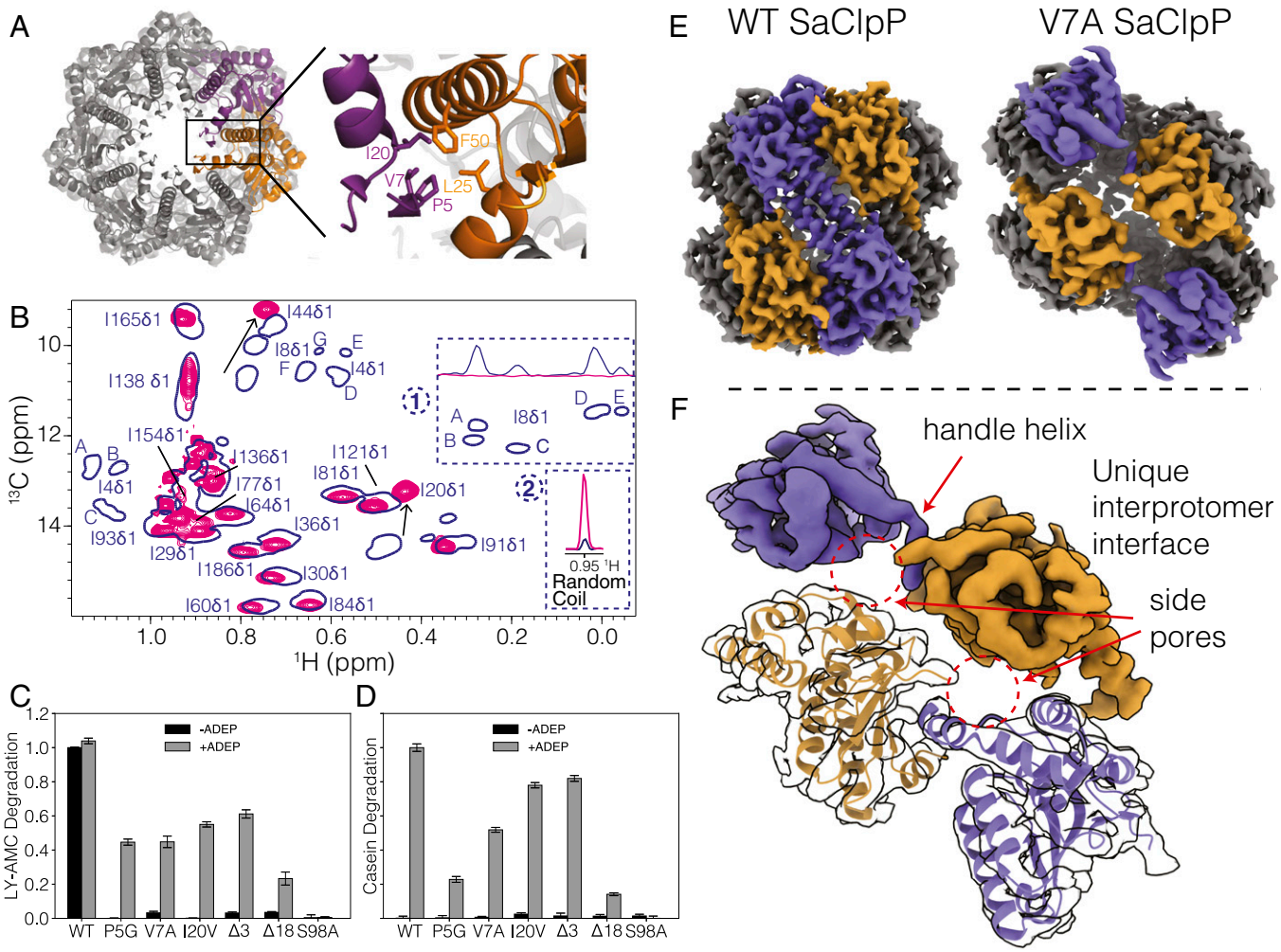

Fig. 4. A conformational hot spot can be manipulated to control ClpP function. (*A*) Cluster of hydrophobic residues at the interface of two adjacent protomers near the apical surface of WT SaClpP [PDB ID code 3V5E (54)] that defines a conformational switch. (*B*) Overlay of the Ile region of ^{1}H-^{13}C HMQC correlation maps of WT SaClpP (blue, single contour) and V7A SaClpP (pink, multiple contours). Note the absence of Ile-4 and Ile-8 peaks (A–E and A–G, respectively) in the V7A spectrum, further highlighted in *Inset 1* showing a projection along the ^{1}H dimension, focusing on peaks from Ile-8. The disappearance of Ile-4 and Ile-8 peaks is coupled with an increase in the intensity of correlations in the random coil region (*Inset 2*). (*C* and *D*) Functional assays probing the activity of various SaClpP constructs using LY-AMC (*C*) and α-casein-FITC (*D*) substrates in the absence (dark bars) or presence (gray bars) of ADEP. Activities are reported relative to WT SaClpP and ADEP-bound WT SaClpP for assays using LY-AMC and α-casein-FITC, respectively. Results are reported as averages and one SD (error bars) from five independent measurements. (*E*) Comparison of 3.6-Å resolution cryo-EM maps of WT and V7A SaClpP; a pair of protomers is colored purple and orange to emphasize the differences in the ring–ring interfaces for the two constructs. (*F*) Close-up view focusing on the interface between purple and orange protomers of V7A SaClpP from *E*, highlighting the sharp bend in the handle helix and its unique interaction with the β-sheet in the head domain of an adjacent protomer.

ClpP degradation chamber and the efficacy of catalysis (Fig. 4*D*). In the absence of the activator ADEP, the P5G, V7A, and I20V mutants, along with constructs with truncated (Δ3) and deleted (Δ18) axial loops, have negligible catalytic activity with the small peptide or casein substrate. The addition of ADEP leads to efficient casein degradation for WT SaClpP, consistent with previous reports (44), and restores at least partial catalysis to all the mutants except the catalytically dead S98A variant, presumably by realigning active-site residues. Taken together, these functional assays demonstrate that the importance of the N-terminal domains goes beyond pore formation, as they are essential for the function and the structural integrity of the tetradecameric ClpP enzyme.

To understand the effect of unfolding the N-terminal β-hairpins from a structural perspective, we determined the cryo-EM structure of V7A SaClpP. Starting from a dataset of 878,240 particle images, a dominant structural class containing 324,522 particle images was obtained in a split-ring conformation that has not been observed before (Fig. 4*E* and *SI Appendix*, Fig. S5). This class of particle images was subsequently used with C2 symmetry to refine a 3D map to 3.7-Å resolution. There are a number of striking differences between the V7A mutant and the WT structures. While six of the seven subunits of a given ring in the V7A structure have a fold similar to that found in the extended form of WT ClpP, one subunit adopts a conformation similar to that of the compact form, in which the handle α-helix has a sharp bend and forms a unique interface with the β-sheet in the head domain of an adjacent protomer (Fig. 4*F*). In this conformation the remaining extended-like protomers are not arranged within the ring in the same manner as for WT SaClpP but rather rise progressively along the circumference of the V7A SaClpP ring (Fig. 4*E*). To accommodate this ∼25-Å rise, these protomers have deviations from the extended form, with a slight unfolding of the N-terminal side of the handle α-helix and a

disruption of the inter-ring β-sheet (*SI Appendix*, Fig. S6). In agreement with the NMR spectrum of the V7A mutant showing that the N-terminal β-hairpins are no longer formed, density is not seen for the β-hairpins in the cryo-EM maps (Fig. 4*E*), indicating that this region is disordered in the mutant. One remarkable feature of the split-ring structure is the formation of a pair of 20-Å-wide pores in the side of the ClpP barrel (Fig. 4*F*). Residues following the catalytic histidine undergo a β-strand (WT) to unfolded (V7A) conformational change, and it is tempting to speculate that this leads to a suboptimal orientation for this important histidine residue that affects catalysis (Fig. 4 *C* and *D*). It is likely that the V7A structure is shared among all the N-terminal mutants discussed above, as 2D class averages from cryo-EM analysis of the Δ3 construct are also consistent with a split-ring conformation (*SI Appendix*, Fig. S6), and the HMQC spectra of all N-terminal mutants are essentially superimposable (*SI Appendix*, Fig. S4), indicating that the N domain is unfolded in each case.

Having established the structural basis for why the V7A SaClpP structure is not catalytically active, we were interested in understanding how binding of ADEP restores activity to this mutant. To this end we obtained a 6.4-Å resolution cryo-EM map of V7A SaClpP bound to ADEP (*SI Appendix*, Figs. S2 and S7). ADEP restores the D7 symmetry of the structure, and the ADEP-bound V7A SaClpP structure resembles the active, extended form of WT SaClpP, with the exception of the N-terminal residues, for which no density is detected (*SI Appendix*, Fig. S7).

The SaClpP Conformational Switch Is Highly Cooperative. Our combined NMR and cryo-EM study establishes that SaClpP is structurally heterogeneous at the level of the N-terminal domain. However, the structural plasticity extends beyond this region with multiple NMR peaks observed for methyl probes throughout the enzyme. Therefore we were interested in examining whether there is crosstalk between protomers that can contribute to this plasticity, and we first used the V7A mutation to address this question. We prepared complexes of SaClpP with different combinations of WT and V7A protomers by unfolding the two proteins separately in guanidine hydrochloride (GdnCl), mixing the two chain types, and with subsequent refolding to generate complexes whose composition and population can be predicted using combinatorial statistics (*SI Appendix*) as described previously (66). ClpP molecules were obtained by mixing subunits in WT:V7A ratios of 50:50%, 85:15%, 90:10%, 95:5%, 98:2%, and 100:0%. For comparison, another set of samples was prepared simply by mixing WT and V7A tetradecamers without any exposure to GdnCl (referred to hereafter as "native mix samples"). The catalytic activities of molecules from both sets of samples were measured relative to a pure WT SaClpP reference using a degradation assay with the LY-AMC substrate (Fig. 5*A*), as described above. The relative activity of the native mix samples (empty circles) was found to be described by a linear function of the fraction of WT ClpP molecules present, as expected for a system consisting of two classes of molecules, one active and the other inactive. By contrast, SaClpP complexes prepared with mixing of unfolded chains lost activity much more rapidly as the V7A protomer content increased (Fig. 5*A*, filled purple circles). The activity profile in this case follows the expected fraction of pure WT complex, WT $ClpP_{14}$, at each mixing ratio ($y = x^{14}$, where x = the percent of WT protomers mixed). These assays provide strong evidence that the presence of a single V7A protomer within an otherwise WT SaClpP tetradecamer is sufficient to generate a catalytically inactive enzyme. In a remarkable example of cooperativity, it appears that breaking a single protomer–protomer interface out of the 14 in a tetradecameric SaClpP ring is adequate to populate the split-ring form.

We next recorded NMR spectra of complexes prepared as 10:90% and 90:10% WT:V7A by mixing unfolded ILVM-labeled

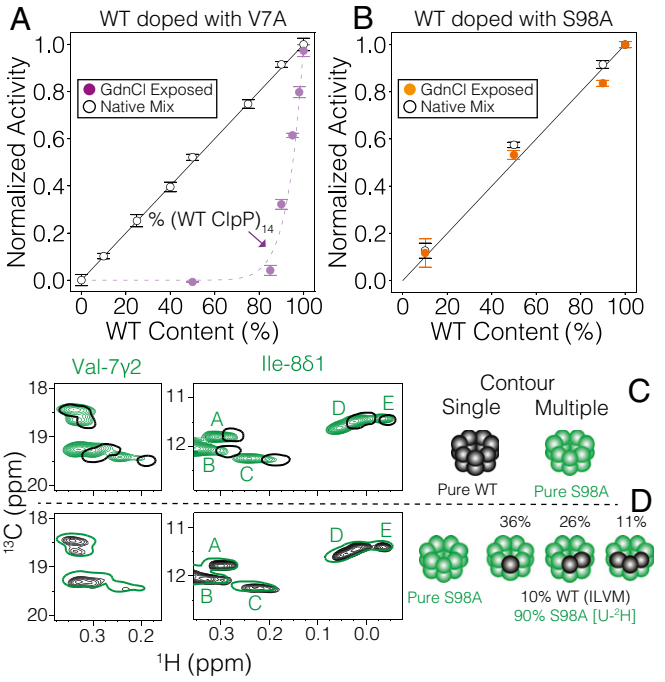

Fig. 5. A V7A mutation in a single protomer is sufficient to trigger N-domain unfolding and eliminate SaClpP catalytic activity. (*A*) Functional assays (LY-AMC hydrolysis) of ClpP complexes prepared with variable numbers of WT and V7A protomers (closed circles, GdnCl exposed) or mixtures of pure WT and V7A 14-mers (open circles, native mix). The solid and dashed lines are the curves $y = x$ and $y = x^{14}$, where x is the percent WT protomer content. (*B*) As in *A* but with V7A protomers replaced by S98A subunits. (*C*) Superposition of selected regions of ^{1}H-^{13}C HMQC spectra of pure WT SaClpP (black, single contour) and pure S98A (green, multicontour) SaClpP. (*D*) Spectral regions as in *C* but focusing on pure S98A ClpP (green, single contour) and a sample with a subunit composition of 10:90% WT:S98A, that was prepared by mixing unfolded protomers and refolding (black, multicontour; only the WT subunits are NMR active). The schematics in *C* and *D* illustrate each species (*C*) or the distribution and populations of the major species (*D*) in solution.

WT protomers with unfolded [U-^{2}H] V7A protomers. Assuming that incorporation of protomers into the tetradecameric complexes is random, the expected populations of pure WT SaClpP are calculated to be ∼0% and 23% for the 10% and 90% WT mixtures, respectively (*SI Appendix*). As described above, we observed a multiplicity of peaks in the pure WT SaClpP sample, in particular for Ile-4 and Ile-8, and we used these peaks as a read-out of the structural properties of the N-terminal gates in the mixture samples that were prepared. This analysis was carried out by recording HMQC spectra for each complex, including for a pure WT sample, and obtaining volume ratios for each Ile-4 and Ile-8 peak ($V_{peak,\ complex}/V_{peak,WT}$; peaks A–E and A–G for Ile-4 and Ile-8, respectively) (Fig. 2*A*), normalized to account for concentration differences in the samples (using intensities of peaks that are not affected by the V7A protomers). The average ratios for the 10:90% and 90:10% WT:V7A samples, 0% and 27 ± 3%, respectively, are in excellent agreement with the estimated fractional populations of pure WT SaClpP, 0% and 23%, respectively. Thus, peaks A–E and A–G for Ile-4 and Ile-8 are direct reporters of ClpP complexes where all protomers are WT only. This conclusion is supported by the fact that the calculated fractional population of molecules with either 13 or 14 WT protomers in a 90:10% WT:V7A sample is 59%, well above the 27% value measured. The absence of N-domain peaks A–E and A–G for all non-WT complexes therefore implies that all N-terminal domains in these ClpP molecules are unfolded, as in

the pure V7A tetradecamer, so that a single V7A protomer is sufficient to unfold the termini, generate the split-ring conformation, and abrogate activity.

As a next step we wondered whether the high degree of cooperativity between neighboring protomers at the level of the conformational switch identified in this study would extend to perturbations of protomer active sites as well. Functional assays similar to those described above for the V7A mutation were performed with native mix and GdnCl unfolded/refolded samples prepared with 10:90%, 50:50%, 90:10%, and 100:0% WT:S98A ratios, where the pure S98A SaClpP enzyme is catalytically dead, Fig. 4 *C* and *D*. Notably, for both types of sample a similar linear correlation between activity and WT protomer content was found, indicating that each WT protomer functions independently in this case (Fig. 5*B*). Nevertheless, NMR experiments indicate that there are subtle changes to the structures of neighboring WT subunits from inactive protomers in the same complex. This observation can be appreciated by first considering the control data of Fig. 5*C* showing superpositions of selective regions of HMQC spectra of pure ILVM-labeled WT (black, single contours) and pure ILVM-S98A (green, multiple contours) SaClpP, highlighting Val-7 and Ile-8 of the N-domain, where there are noticeable changes in the multiple peaks that derive from these residues. We next prepared a sample of SaClpP by mixing 10% unfolded ILVM-WT and 90% unfolded ^{2}H-labeled S98A protomers followed by refolding (only WT protomers are NMR active). The NMR spectrum (Fig. 5*D*) was much more similar to that of pure S98A ClpP than that of the pure WT state, consistent with small changes in the N-domain structure of the WT protein (more S98A-like) that derive from the S98A mutations in the active sites of adjacent protomers. These changes are not the result of the unfolding/refolding protocol used to prepare the sample, as identical spectra (and functional activities) were obtained from WT ClpP samples that were prepared with or without the initial unfolding/refolding step. Thus, while the S98A mutation evokes subtle changes to the conformations of the N-terminal domains of neighboring subunits, providing a further illustration of the plasticity of the ClpP structure, these appear not to be of functional consequence.

Conformational Heterogeneity Is a General Feature of ClpPs. We next sought to establish whether the observed heterogeneity in the N-terminal region of SaClpP is also present in ClpPs from other organisms using a simple NMR approach. Rather than use the ILVM-labeling strategy described above in the context of SaClpP for which chemical shift assignments would then be required, we used a faster method, albeit one that provides information about only a single site. To this end, a single Cys mutation was introduced into ClpP from *E. coli* (EcClpP) and *N. meningitidis* (NmClpP) at positions analogous to Thr-6 in SaClpP (M5C and T10C in EcClpP and NmClpP, respectively). Highly deuterated protein was produced and subsequently reacted with ^{13}C-methyl-methanethiosulfonate (MMTS) that led to the attachment of a $^{13}CH_3$–S group to the introduced Cys sidechain, forming an S-methylthio-cysteine (MTC) residue (67). In this way a single methyl probe localized to the N-terminal domain becomes available to assess the conformational heterogeneity of this region. Fig. 6 shows ^{1}H-^{13}C HMQC spectra of EcClpP MTC5 (Fig. 6*A*) and NmClpP MTC10 (Fig. 6*B*), establishing that the N-terminal regions of both proteins are structurally heterogeneous based on the large number of observed correlations derived from a single methyl group (blue contours). Similar to SaClpP, the structural heterogeneity is significantly reduced in V6A (EcClpP) and V11A (NmClpP) mutated proteins (red contours), where positions 6 (EcClpP) and 11 (NmClpP) are equivalent to position 7 in SaClpP.

Having shown that heterogeneity can be manipulated in the EcClpP and NmClpP systems as in SaClpP, we next asked whether the catalytic activity would be similarly reduced in the Val-to-Ala mutants of EcClpP and NmClpP described above. Degradation assays were performed using both LY-AMC and α-casein substrates. As shown in Fig. 6 *C* and *D*, V11A NmClpP is catalytically inactive but becomes activated upon ADEP addition although still less than for WT bound with ADEP. Similar results were obtained for EcClpP (Fig. 6 *E* and *F*), although, unlike NmClpP, the mutation does not fully eliminate the EcClpP activity against LY-AMC, and the addition of ADEP renders the mutant as active as WT for peptide degradation.

Discussion

ClpP proteases have emerged as important targets for the development of new classes of antibiotics against bacterial infections (13–15, 17, 18, 68) and for the design of antimalarial agents (20). In humans, ClpP plays a role in the mitochondrial unfolded protein response (69), and its inhibition provides a potential avenue for treating acute myeloid leukemia (22). The implications of regulating ClpP function are further underscored by a recent set of experiments whereby ClpP-knockout mice were

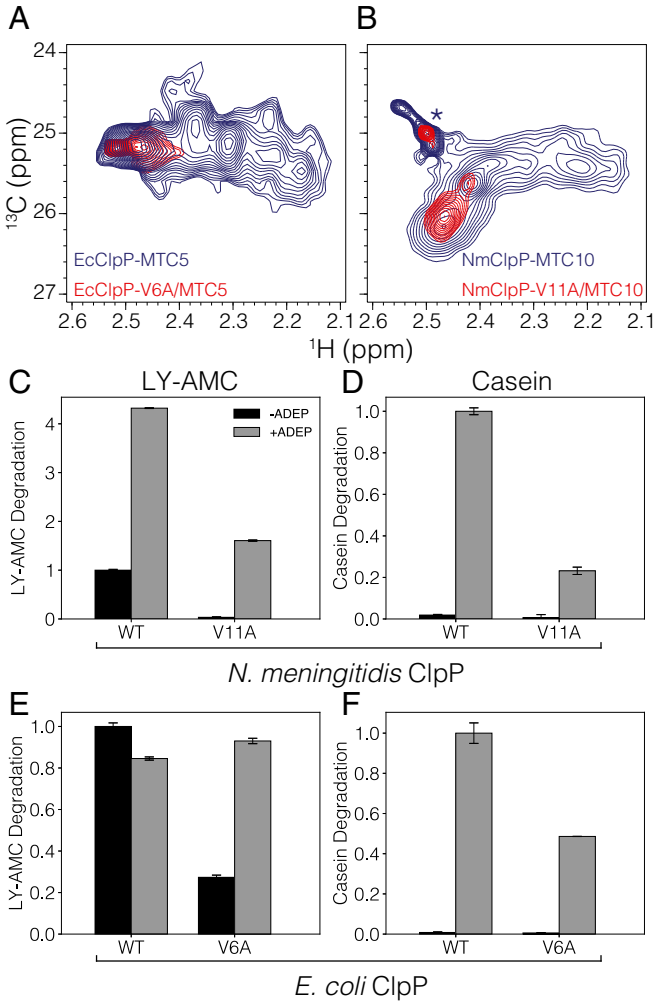

Fig. 6. N-domain conformational heterogeneity is a general feature of ClpPs. (*A* and *B*) Superposition of ^{1}H-^{13}C HMQC spectra of *E. coli* (*A*) and *N. meningitidis* (*B*) ClpP that have been reacted with MMTS to generate single $^{13}CH_3$ probes at homologous positions 5 and 10, respectively. Many correlations are observed in each case (blue). The spectra are simplified (with a single predominant peak, red) for V6A (*E. coli*, *A*) and V11A (*N. meningitides*, *B*) substitutions that correspond to the V7A mutation for SaClpP. The peak with an asterisk in *B* derives from a cleaved label. (*C*–*F*) Activity assays for WT and mutated NmClpP (*C* and *D*) and EcClpP (*E* and *F*), without (black bars) and with (gray bars) ADEP.

protected against obesity when administered a fat-rich diet (70). The biomedical importance of this enzyme and the potential for manipulating its function through the design of new small-molecule modulators have led to efforts to understand the relationship among ClpP structure, dynamics, and function (13). Biophysical studies have established that ClpP is a highly plastic structure (32, 36, 44, 71), suggesting that it may be possible to manipulate its function by exploiting its conformational flexibility. Indeed, such an approach was used recently in the development of the ADEP and ACP regulators, where binding of these compounds leads to an open state of the axial pores and consequently to up-regulation of activity (14, 15). By contrast, β-lactones and phenyl esters operate via direct chemical modification of the catalytic Ser (72, 73). However, inhibiting the function of ClpP by taking advantage of its plasticity remains mostly unexplored.

In an effort to better understand the relationship between plasticity and function in the ClpP enzyme system, we have used a combined NMR, biochemical, and cryo-EM approach, focusing primarily on the protein from *S. aureus* that gives superior-quality NMR spectra relative to other ClpPs that we examined. We have found that the N-terminal domain is structurally heterogeneous. This conclusion is made clear by the multiplicity of cross-peaks in NMR spectra, especially for residues localized to the N terminus, where close to 10 separate resonances each are found for Ile-4 and Ile-8, suggesting at least that number of separate conformers. These conformers are structurally diverse, with a distribution of distances ranging from ∼23–34 Å between Ile-4 and Ile-8 probes and Gln-130 (the point of attachment of a spin label in PRE experiments) and different Ile δ2 χ_2 rotameric states as calculated from $^{13}C^{\delta1}$ chemical shifts (Fig. 2). The heterogeneity at the level of the N terminus is further established from the cryo-EM structure of the WT form of SaClpP, showing a resolution of ∼6 Å for this region relative to the other parts of the protein. To evaluate the flexibility of the N-domain further, we performed a restrained MD simulation that generates an ensemble of structures that explain the cryo-EM density better than a single conformation (*SI Appendix*, Fig. S8). The N-terminal domains of the resulting structures show considerable variability in the sidechain positions of the residues for which peak multiplicity was observed in NMR spectra. For example, variations in the distance between the Cδ1 atoms of Ile-4 and Ile-8 and the particle center of mass range over 9 Å in the ensemble. Importantly, however, all the structures place the sidechain of Val-7 inside a hydrophobic cluster, interacting with Pro-5 and Ile-20 from the same protomer and Leu-25 and Phe-50 from an adjacent subunit, that is more rigidly positioned in the ensemble than Ile-4 and Ile-8. This hydrophobic cluster has been shown to be important in stabilizing the active conformation of the enzyme.

Our NMR and cryo-EM results therefore paint a picture in which the N-terminal domains of SaClpP are structurally heterogeneous but are critical for function. Mutations such as P5G, V7A, and I20V or deletions of as few as the first three residues after Met-1 are sufficient to unfold the N-domain and abrogate catalytic activity (Fig. 4), while the addition of ADEP at least partially restores catalysis. The cryo-EM structure of V7A SaClpP shows that the dominant structured class is strikingly different from that of WT SaClpP, with a split-ring structure formed that is reminiscent of conformers recently determined for a number of AAA+ proteins (74–77). Notably, the interfaces between two pairs of protomers are remodeled in the V7A complex with a shortened and kinked handle helix from one subunit contacting the head domain of an adjacent protomer, generating a pair of 20-Å-wide side-pores (Fig. 4). In an effort to understand how product efflux from the ClpP lumen might occur, Sieber and coworkers (54) speculated about the presence of ClpP tetradecamers where two protomers of SaClpP in the active, extended conformation are replaced by monomers in the compressed state, forming extended side-pores similar to those observed in our experimentally defined structure. However, it remains to be established whether such pores are formed during the catalytic cycle so as to potentially expedite removal of product. Although the resolution of the V7A SaClpP cryo-EM map is not sufficient to accurately place the catalytic residues in the structure, the observed secondary structure transition from β-sheet to coil in the immediate vicinity of the active-site histidine residue provides a likely explanation for the elimination of activity, with ADEP binding restoring the overall WT structure and much of catalysis. Remarkably, a single V7A substitution in only one of the 14 protomers of SaClpP is sufficient to unfold the termini of all subunits and abrogate catalysis, establishing a strong coupling between the N-terminal domains of the different protomers. A structural hotspot is thus identified involving a hydrophobic patch that includes Val-7. The importance of this residue is further underscored by the preservation of interactions involving Val-7 in all WT SaClpP structures obtained from a cryo-EM–restrained MD ensemble, even though considerable distance fluctuations were noted in surrounding sidechains, as discussed above.

Protein hydrolysis is critical for proper cellular function (1, 78), and the key protease components of each protein degradation system must be highly regulated to ensure that only proper substrates are degraded. This is achieved at a global level by sequestration of the active sites within a gated barrel and by the binding of large regulatory particles, such as unfoldases, that unfold properly tagged substrates to facilitate their entry into the lumen of the protease (79, 80). Further levels of control can be achieved via a number of allosteric hotspots that exploit the conformational plasticity of the protease to modulate its activity (81), as in ClpP. Here, coordination between ClpP and its partner AAA+ unfoldases is mediated by hydrophobic binding pockets at the interfaces between pairs of ClpP protomers that form the docking sites for the unfoldase and that communicate unfoldase binding to the catalytic sites in the enzyme (44). The ADEP and ACP classes of antibiotic candidates, as well as certain mutations, take advantage of this binding pocket to cause unregulated ClpP activity by pore opening and allosteric conformational changes that propagate to the active site (15, 43, 45). Another important hotspot is the oligomerization sensor that comprises Asp-170 and Arg-171. The Asp-170–Arg-171 pair from one protomer is connected via salt bridges to the corresponding pair in the opposite ring, stabilizing the active extended conformation and thereby coupling oligomerization with catalysis. Sieber and coworkers (44) have shown that mutations to this region trap SaClpP in the inactive compressed form, with ADEP binding restoring activity by selecting for the extended form of the enzyme, demonstrating the communication between the hydrophobic binding pocket and the oligomerization sensor hotspots. The N-terminal switch discovered in the present work adds to the list of sites that exert conformational and functional control over ClpP.

That a single V7A mutation in only one protomer is sufficient to generate large structural and functional changes in SaClpP supports the notion that the free energy landscape of this complex is rugged, with different conformers becoming accessible through the binding of regulators, drug molecules, or mutations. The resulting inherent plasticity may play a role in regulating ClpP activity through the hotspots discussed above and via allosteric pathways that connect unfoldase binding with increased protease activity, e.g., fine-tuning enzyme function. The hotspot identified in this work serves as an intriguing target for allosteric inhibition of ClpP. Notably, our studies of the S98A:WT mixed SaClpP complex establish that the active sites of each protomer function independently so that complete inhibition by compounds binding to active sites can be achieved only by targeting all 14 subunits. In contrast, because destabilization of only one of the 14 hydrophobic clusters identified presently is sufficient to eliminate proteolysis for SaClpP, targeting these sites may prove to be easier than or an important complementary strategy to the use of active-site inhibitors.

Materials and Methods

ClpP proteins were prepared as described in *SI Appendix*. All NMR measurements were performed at 18.8 T and 40 °C unless indicated otherwise, using Varian Inova or Bruker AVANCE III HD spectrometers equipped with room-temperature (Varian) or cryogenically cooled (Bruker) pulsed-field gradient triple-resonance probes. ^{1}H-^{13}C correlation spectra were recorded as HMQC datasets, exploiting a methyl-TROSY effect that is particularly beneficial for applications to high molecular weight proteins (48). Spectra were processed using the NMRPipe suite of programs (82), analyzed using scripts written in-house, and visualized using Ccpnmr (83) and Nmrglue packages (84).

ACKNOWLEDGMENTS. We thank Dr. R. Muhandiram, Dr. R. Huang, and Dr. Samir Benlekbir for help with NMR, production of mixed ClpP complexes, and cryo-EM data collection on the Titan Krios, respectively. This work was supported by grants from the Canadian Institutes of Health Research (CIHR) (to W.A.H., J.L.R., and L.E.K.) and the Natural Sciences and Engineering Research Council of Canada (to J.L.R. and L.E.K.). S.V. and T.Y. were supported by CIHR postdoctoral fellowships, and Z.A.R. was supported by a SickKids ResTraComp Scholarship and an Ontario Graduate Scholarship. J.L.R. and L.E.K. are recipients of Canada Research Chairs. Titan Krios cryo-EM data were collected at the Toronto High-Resolution High-Throughput cryo-EM facility supported by the Canadian Foundation for Innovation and Ontario Research Fund.

1. Olivares AO, Baker TA, Sauer RT (2016) Mechanistic insights into bacterial AAA+ proteases and protein-remodelling machines. *Nat Rev Microbiol* 14:33–44.
2. Kress W, Maglica Z, Weber-Ban E (2009) Clp chaperone-proteases: Structure and function. *Res Microbiol* 160:618–628.
3. Lupas A, Flanagan JM, Tamura T, Baumeister W (1997) Self-compartmentalizing proteases. *Trends Biochem Sci* 22:399–404.
4. Liu K, Ologbenla A, Houry WA (2014) Dynamics of the ClpP serine protease: A model for self-compartmentalized proteases. *Crit Rev Biochem Mol Biol* 49:400–412.
5. Alexopoulos JA, Guarné A, Ortega J (2012) ClpP: A structurally dynamic protease regulated by AAA+ proteins. *J Struct Biol* 179:202–210.
6. Dougan DA (2013) *Regulated Proteolysis in Microorganisms* (Springer, Dordrecht, The Netherlands).
7. Gaillot O, Pellegrini E, Bregenholt S, Nair S, Berche P (2000) The ClpP serine protease is essential for the intracellular parasitism and virulence of Listeria monocytogenes. *Mol Microbiol* 35:1286–1294.
8. Michalik S, et al. (2012) Life and death of proteins: A case study of glucose-starved Staphylococcus aureus. *Mol Cell Proteomics* 11:558–570.
9. Zhao BB, Li XH, Zeng YL, Lu YJ (2016) ClpP-deletion impairs the virulence of Legionella pneumophila and the optimal translocation of effector proteins. *BMC Microbiol* 16: 174.
10. Foster TJ (2017) Antibiotic resistance in Staphylococcus aureus. Current status and future prospects. *FEMS Microbiol Rev* 41:430–449.
11. Culp E, Wright GD (2017) Bacterial proteases, untapped antimicrobial drug targets. *J Antibiot (Tokyo)* 70:366–377.
12. Malik IT, Brötz-Oesterhelt H (2017) Conformational control of the bacterial Clp protease by natural product antibiotics. *Nat Prod Rep* 34:815–831.
13. Ye F, Li J, Yang CG (2016) The development of small-molecule modulators for ClpP protease activity. *Mol Biosyst* 13:23–31.
14. Kirstein J, et al. (2009) The antibiotic ADEP reprogrammes ClpP, switching it from a regulated to an uncontrolled protease. *EMBO Mol Med* 1:37–49.
15. Leung E, et al. (2011) Activators of cylindrical proteases as antimicrobials: Identification and development of small molecule activators of ClpP protease. *Chem Biol* 18: 1167–1178.
16. Sass P, et al. (2011) Antibiotic acyldepsipeptides activate ClpP peptidase to degrade the cell division protein FtsZ. *Proc Natl Acad Sci USA* 108:17474–17479.
17. Raju RM, Goldberg AL, Rubin EJ (2012) Bacterial proteolytic complexes as therapeutic targets. *Nat Rev Drug Discov* 11:777–789.
18. Conlon BP, et al. (2013) Activated ClpP kills persisters and eradicates a chronic biofilm infection. *Nature* 503:365–370.
19. Zeiler E, Korotkov VS, Lorenz-Baath K, Böttcher T, Sieber SA (2012) Development and characterization of improved β-lactone-based anti-virulence drugs targeting ClpP. *Bioorg Med Chem* 20:583–591.
20. Mundra S, et al. (2017) A novel class of plasmodial ClpP protease inhibitors as potential antimalarial agents. *Bioorg Med Chem* 25:5662–5677.
21. Seo JH, et al. (2016) The mitochondrial unfoldase-peptidase complex ClpXP controls bioenergetics stress and metastasis. *PLoS Biol* 14:e1002507.
22. Cole A, et al. (2015) Inhibition of the mitochondrial protease ClpP as a therapeutic strategy for human acute myeloid leukemia. *Cancer Cell* 27:864–876.
23. Jenkinson EM, et al.; University of Washington Center for Mendelian Genomics (2013) Perrault syndrome is caused by recessive mutations in CLPP, encoding a mitochondrial ATP-dependent chambered protease. *Am J Hum Genet* 92:605–613.
24. Pierce SB, et al. (2013) Mutations in LARS2, encoding mitochondrial leucyl-tRNA synthetase, lead to premature ovarian failure and hearing loss in Perrault syndrome. *Am J Hum Genet* 92:614–620.
25. Wang J, Hartling JA, Flanagan JM (1997) The structure of ClpP at 2.3 A resolution suggests a model for ATP-dependent proteolysis. *Cell* 91:447–456.
26. Kang SG, Maurizi MR, Thompson M, Mueser T, Ahvazi B (2004) Crystallography and mutagenesis point to an essential role for the N-terminus of human mitochondrial ClpP. *J Struct Biol* 148:338–352.
27. Kim DY, Kim KK (2008) The structural basis for the activation and peptide recognition of bacterial ClpP. *J Mol Biol* 379:760–771.
28. Bewley MC, Graziano V, Griffin K, Flanagan JM (2006) The asymmetry in the mature amino-terminus of ClpP facilitates a local symmetry match in ClpAP and ClpXP complexes. *J Struct Biol* 153:113–128.
29. Kim Y-I, Burton RE, Burton BM, Sauer RT, Baker TA (2000) Dynamics of substrate denaturation and translocation by the ClpXP degradation machine. *Mol Cell* 5: 639–648.
30. Ortega J, Singh SK, Ishikawa T, Maurizi MR, Steven AC (2000) Visualization of substrate binding and translocation by the ATP-dependent protease, ClpXP. *Mol Cell* 6: 1515–1521.
31. Geiger SR, Böttcher T, Sieber SA, Cramer P (2011) A conformational switch underlies ClpP protease function. *Angew Chem Int Ed Engl* 50:5749–5752.
32. Kimber MS, et al. (2010) Structural and theoretical studies indicate that the cylindrical protease ClpP samples extended and compact conformations. *Structure* 18:798–808.
33. Ye F, et al. (2013) Helix unfolding/refolding characterizes the functional dynamics of Staphylococcus aureus Clp protease. *J Biol Chem* 288:17643–17653.
34. Lee B-G, Kim MK, Song HK (2011) Structural insights into the conformational diversity of ClpP from Bacillus subtilis. *Mol Cells* 32:589–595.
35. Díaz-Sáez L, Pankov G, Hunter WN (2017) Open and compressed conformations of Francisella tularensis ClpP. *Proteins* 85:188–194.
36. Sprangers R, Gribun A, Hwang PM, Houry WA, Kay LE (2005) Quantitative NMR spectroscopy of supramolecular complexes: Dynamic side pores in ClpP are important for product release. *Proc Natl Acad Sci USA* 102:16678–16683.
37. Zhang J, et al. (2011) Structural switching of Staphylococcus aureus Clp protease: A key to understanding protease dynamics. *J Biol Chem* 286:37590–37601.
38. Lee B-G, et al. (2010) Structures of ClpP in complex with acyldepsipeptide antibiotics reveal its activation mechanism. *Nat Struct Mol Biol* 17:471–478.
39. Jennings LD, Lun DS, Médard M, Licht S (2008) ClpP hydrolyzes a protein substrate processively in the absence of the ClpA ATPase: Mechanistic studies of ATP-independent proteolysis. *Biochemistry* 47:11536–11546.
40. Thompson MW, Singh SK, Maurizi MR (1994) Processive degradation of proteins by the ATP-dependent Clp protease from Escherichia coli. Requirement for the multiple array of active sites in ClpP but not ATP hydrolysis. *J Biol Chem* 269:18209–18215.
41. Martin A, Baker TA, Sauer RT (2007) Distinct static and dynamic interactions control ATPase-peptidase communication in a AAA+ protease. *Mol Cell* 27:41–52.
42. Baytshtok V, Baker TA, Sauer RT (2015) Assaying the kinetics of protein denaturation catalyzed by AAA+ unfolding machines and proteases. *Proc Natl Acad Sci USA* 112: 5377–5382.
43. Sowole MA, Alexopoulos JA, Cheng Y-Q, Ortega J, Konermann L (2013) Activation of ClpP protease by ADEP antibiotics: Insights from hydrogen exchange mass spectrometry. *J Mol Biol* 425:4508–4519.
44. Gersch M, et al. (2015) AAA+ chaperones and acyldepsipeptides activate the ClpP protease via conformational control. *Nat Commun* 6:6320.
45. Ni T, et al. (2016) Characterization of gain-of-function mutant provides new insights into ClpP structure. *ACS Chem Biol* 11:1964–1972.
46. Tugarinov V, Kay LE (2004) An isotope labeling strategy for methyl TROSY spectroscopy. *J Biomol NMR* 28:165–172.
47. Kerfah R, Plevin MJ, Sounier R, Gans P, Boisbouvier J (2015) Methyl-specific isotopic labeling: A molecular tool box for solution NMR studies of large proteins. *Curr Opin Struct Biol* 32:113–122.
48. Tugarinov V, Hwang PM, Ollerenshaw JE, Kay LE (2003) Cross-correlated relaxation enhanced 1H[bond]13C NMR spectroscopy of methyl groups in very high molecular weight proteins and protein complexes. *J Am Chem Soc* 125:10420–10428.
49. Rosenzweig R, Kay LE (2014) Bringing dynamic molecular machines into focus by methyl-TROSY NMR. *Annu Rev Biochem* 83:291–315.
50. Jiang Y, Kalodimos CG (2017) NMR studies of large proteins. *J Mol Biol* 429: 2667–2676.
51. Bonomi M, Camilloni C, Cavalli A, Vendruscolo M (2016) Metainference: A Bayesian inference method for heterogeneous systems. *Sci Adv* 2:e1501177.
52. Bonomi M, Pellarin R, Vendruscolo M (2018) Simultaneous determination of protein structure and dynamics using cryo-electron microscopy. *Biophys J* 114:1604–1613.
53. Sprangers R, Kay LE (2007) Quantitative dynamics and binding studies of the 20S proteasome by NMR. *Nature* 445:618–622.
54. Gersch M, List A, Groll M, Sieber SA (2012) Insights into structural network responsible for oligomerization and activity of bacterial virulence regulator caseinolytic protease P (ClpP) protein. *J Biol Chem* 287:9484–9494.
55. Gans P, et al. (2010) Stereospecific isotopic labeling of methyl groups for NMR spectroscopic studies of high-molecular-weight proteins. *Angew Chem Int Ed Engl* 49: 1958–1962.
56. Hansen DF, Neudecker P, Kay LE (2010) Determination of isoleucine side-chain conformations in ground and excited states of proteins from chemical shifts. *J Am Chem Soc* 132:7589–7591.
57. Religa TL, Sprangers R, Kay LE (2010) Dynamic regulation of archaeal proteasome gate opening as studied by TROSY NMR. *Science* 328:98–102.
58. Vallurupalli P, Bouvignies G, Kay LE (2012) Studying "invisible" excited protein states in slow exchange with a major state conformation. *J Am Chem Soc* 134:8148–8161.
59. Sun H, Kay LE, Tugarinov V (2011) An optimized relaxation-based coherence transfer NMR experiment for the measurement of side-chain order in methyl-protonated, highly deuterated proteins. *J Phys Chem B* 115:14878–14884.

60. Mittermaier A, Kay LE, Forman-Kay JD (1999) Analysis of deuterium relaxation-derived methyl axis order parameters and correlation with local structure. *J Biomol NMR* 13:181–185.
61. Punjani A, Rubinstein JL, Fleet DJ, Brubaker MA (2017) cryoSPARC: Algorithms for rapid unsupervised cryo-EM structure determination. *Nat Methods* 14:290–296.
62. Cardone G, Heymann JB, Steven AC (2013) One number does not fit all: Mapping local variations in resolution in cryo-EM reconstructions. *J Struct Biol* 184:226–236.
63. Bonomi M, Camilloni C, Vendruscolo M (2016) Metadynamic metainference: Enhanced sampling of the metainference ensemble using metadynamics. *Sci Rep* 6: 31232.
64. Trabuco LG, Villa E, Mitra K, Frank J, Schulten K (2008) Flexible fitting of atomic structures into electron microscopy maps using molecular dynamics. *Structure* 16: 673–683.
65. Han B, Liu Y, Ginzinger SW, Wishart DS (2011) SHIFTX2: Significantly improved protein chemical shift prediction. *J Biomol NMR* 50:43–57.
66. Huang R, Pérez F, Kay LE (2017) Probing the cooperativity of *Thermoplasma acidophilum* proteasome core particle gating by NMR spectroscopy. *Proc Natl Acad Sci USA* 114:E9846–E9854.
67. Religa TL, Ruschak AM, Rosenzweig R, Kay LE (2011) Site-directed methyl group labeling as an NMR probe of structure and dynamics in supramolecular protein systems: Applications to the proteasome and to the ClpP protease. *J Am Chem Soc* 133: 9063–9068.
68. Raju RM, et al. (2012) Mycobacterium tuberculosis ClpP1 and ClpP2 function together in protein degradation and are required for viability in vitro and during infection. *PLoS Pathog* 8:e1002511.
69. Haynes CM, Petrova K, Benedetti C, Yang Y, Ron D (2007) ClpP mediates activation of a mitochondrial unfolded protein response in C. elegans. *Dev Cell* 13:467–480.
70. Bhaskaran S, et al. (2018) Loss of mitochondrial protease ClpP protects mice from diet-induced obesity and insulin resistance. *EMBO Rep* 19:e45009.
71. Li M, et al. (2016) Structure and functional properties of the active form of the proteolytic complex, ClpP1P2, from Mycobacterium tuberculosis. *J Biol Chem* 291: 7465–7476.
72. Böttcher T, Sieber SA (2008) β-lactones as privileged structures for the active-site labeling of versatile bacterial enzyme classes. *Angew Chem Int Ed Engl* 47:4600–4603.
73. Hackl MW, et al. (2015) Phenyl esters are potent inhibitors of caseinolytic protease P and reveal a stereogenic switch for deoligomerization. *J Am Chem Soc* 137: 8475–8483.
74. Zhao M, et al. (2015) Mechanistic insights into the recycling machine of the SNARE complex. *Nature* 518:61–67.
75. Huang R, et al. (2016) Unfolding the mechanism of the AAA+ unfoldase VAT by a combined cryo-EM, solution NMR study. *Proc Natl Acad Sci USA* 113:E4190–E4199.
76. Monroe N, Han H, Shen PS, Sundquist WI, Hill CP (2017) Structural basis of protein translocation by the Vps4-Vta1 AAA ATPase. *eLife* 6:e24487.
77. Gates SN, et al. (2017) Ratchet-like polypeptide translocation mechanism of the AAA+ disaggregase Hsp104. *Science* 357:273–279.
78. Goldberg AL (2003) Protein degradation and protection against misfolded or damaged proteins. *Nature* 426:895–899.
79. Lee ME, Baker TA, Sauer RT (2010) Control of substrate gating and translocation into ClpP by channel residues and ClpX binding. *J Mol Biol* 399:707–718.
80. Effantin G, Maurizi MR, Steven AC (2010) Binding of the ClpA unfoldase opens the axial gate of ClpP peptidase. *J Biol Chem* 285:14834–14840.
81. Ruschak AM, Kay LE (2012) Proteasome allostery as a population shift between interchanging conformers. *Proc Natl Acad Sci USA* 109:E3454–E3462.
82. Delaglio F, et al. (1995) NMRPipe: A multidimensional spectral processing system based on UNIX pipes. *J Biomol NMR* 6:277–293.
83. Vranken WF, et al. (2005) The CCPN data model for NMR spectroscopy: Development of a software pipeline. *Proteins* 59:687–696.
84. Helmus JJ, Jaroniec CP (2013) Nmrglue: An open source Python package for the analysis of multidimensional NMR data. *J Biomol NMR* 55:355–367.